RESEARCH ARTICLE
SOLID EARTH: GEODYNAMICS

Earth and Planetary Physics
10: 497–511, 2026
doi: 10.26464/epp2026041

An improved edge detection method for interpreting gravity potential field data

ZhiXin Xue[1], Lei Jing[1*], YaBin Yang[1], MengLong Xu[1], LongJun Qiu[1], ChengYe Sun[1], SuLi Shi[1], ZhenNing Su[1], and Jian Fang[2]

[1]Institute of Geophysical and Geochemical Exploration, Chinese Academy of Geological Sciences, Tianjin 300309, China;

[2]State Key Laboratory of Precision Geodesy, Innovation Academy for Precision Measurement Science and Technology, Chinese Academy of Sciences, Wuhan 430077, China

Key Points:

- An improved high-resolution boundary identification method is proposed.
- This method provides high-resolution tectonic constraints for the South China Sea.

Citation: Xue, Z. X., Jing, L., Yang, Y. B., Xu, M. L., Qiu, L. J., Sun, C. Y., Shi, S. L., Su, Z. N., and Fang, J. (2026). An improved edge detection method for interpreting gravity potential field data. *Earth Planet. Phys.*, *10*(3), 497–511. http://doi.org/10.26464/epp2026041

Abstract: Edge detection represents a critical task in potential field data interpretation and is extensively utilized for detecting faults, contacts, and other linear geological structures. However, conventional methods are constrained by several limitations, including inadequate balancing of signals with varying amplitude intensities, dispersed detection results, and insufficient suppression of spurious signals. To overcome these challenges, we propose an improved edge detection method, designated as the hyperbolic tangent (TANH) function with Gaussian envelope constraints on the total gradient modulus tilt angle (THASTG). The THASTG method is formally defined as a tilt angle approach based on the total gradient modulus, incorporating dual constraints through a Gaussian envelope and a TANH function. We initially conducted comparative analyses between the THASTG and established methods by using complex models simulating three distinct geological scenarios, thereby validating the feasibility of the methodology. Subsequent application to real gravity data from the South China Sea region demonstrated that compared with conventional techniques, THASTG yields enhanced structural detail, improved boundary resolution, and superior noise suppression. This method effectively suppresses noise interference and successfully avoids the introduction of spurious boundaries while maintaining consistency with previously documented major tectonic features. This study provides high-resolution structural constraints for the South China Sea region, delineates the offshore extension of the Red River Fault system, and accurately maps the continent–ocean boundary configuration. Our results demonstrate that the proposed methodology provides an effective tool for precise structural characterization and in-depth analysis of geodynamic evolution processes.

Keywords: edge detection; potential field data; gravity anomaly; South China Sea

1. Introduction

Gravity field edge detection is a primary task in gravity data interpretation and is used to identify the boundaries of subsurface geological structures. This technique leverages density contrasts between different geological bodies or structural elements to enhance characteristic variations in the gravity field caused by these differences, thereby enabling precise delineation of lateral structural changes. Owing to its high processing efficiency and sensitivity to boundary responses, gravity edge detection has become an important tool for identifying fault structures, analyzing basin boundaries, and studying deep geological features. It provides critical evidence for revealing regional geological frameworks and dynamic processes (Paterson and Reeves, 1985; Xue ZX et al., 2021).

Conventional edge detection methods are primarily based on transformations of the gravity field and its derivatives. Techniques such as the vertical derivative, total horizontal derivative, and analytic signal amplitude have been widely employed to delineate source boundaries and serve as common tools for interpreting density contacts (Cordell, 1979; Cordell and Grauch, 1982; Roest et al., 1992). Subsequent developments, such as the tilt angle method (Miller and Singh, 1994), further improved the accuracy of edge localization and significantly enhanced the balanced detection of anomalies with varying amplitudes. However, these conventional approaches exhibit notable limitations when dealing with multisource superimposed fields or geological bodies at different depths, often failing to clearly resolve both shallow and deep structural boundaries simultaneously and remaining suscep-

First author: Z. X. Xue, xzxg25@163.com
Correspondence to: L. Jing, corzx25@163.com
Received 03 NOV 2025; Accepted 02 MAR 2026.

tible to noise (Beiki, 2010; Yuan Y et al., 2016). To address these shortcomings, a series of phase-based methods have been developed, including the tilt angle of the total horizontal derivative (Verduzco et al., 2004), the theta map (Wijns et al., 2005), and the normalized horizontal tilt angle (Cooper and Cowan, 2006). These methods achieve a more balanced recognition of strong and weak anomalies to some extent; however, they remain prone to spurious boundaries and noise interference (Eldosouky et al., 2020). In recent years, the performance of edge detection has been further improved through the use of strategies such as higher order derivatives, image processing techniques, and algorithms incorporating activation functions (Sertcelik and Kafadar, 2012; Zhang X et al., 2015; Pham et al., 2020, 2022). Concurrently, deep learning methods have demonstrated strong feature learning capabilities when sufficient data are available (Zhou S et al., 2024; Zhou XY et al., 2024), while progress in adaptive filtering has enhanced local noise suppression (Ferreira et al., 2013). However, these approaches still commonly face limitations, including reliance on data and insufficient interpretability. A particular ongoing challenge within traditional gradient-based methods is how to effectively suppress noise and avoid spurious boundaries without compromising resolution (Xue ZX et al., 2025a). Nevertheless, critical challenges persist, including the proliferation of false boundaries, the difficulty of simultaneously achieving high resolution and noise robustness, and effective noise suppression (Zhang X et al., 2015; Pham et al., 2020, 2022).

Building on existing research, this work utilizes the hyperbolic tangent (TANH)-based method with Gaussian envelope constraints on the tilt angle of the total gradient modulus (THASTG) to delineate horizontal geological boundaries. This approach effectively balances amplitude variations across different depths, suppresses noise interference, and yields higher resolution detection results. It provides enhanced imaging details, achieves high identification accuracy, and minimizes the introduction of spurious anomalies. The reliability and noise resistance of THASTG are validated through synthetic datasets, including single positive anomalies, positive–negative composite anomalies, and noisy composite anomalies, demonstrating its robustness under complex scenarios. Furthermore, this method is successfully applied to gravity data from the South China Sea region, where it identifies 20 fault zones on the basis of integrated gravity field model data, clarifies the extension characteristics of the Red River Fault Zone, and accurately delineates the continent–ocean boundary with improved structural clarity and convergence. These results not only align consistently with those of previous studies but also provide new high-precision structural information, offering critical insights for further analysis of regional tectonic activity.

2. Methods

The total horizontal gradient (THG), introduced by Cordell (1979), is utilized to delineate the boundaries of geological sources. The THG is defined as follows:

$$\mathrm{THG} = \sqrt{G_{xz}^2 + G_{yz}^2}, \tag{1}$$

where the gradients of the gravity anomaly G_g in the x and y directions are G_{xz} and G_{yz}, respectively.

The analytical signal amplitude (ASA) filter, introduced by Roest et al. (1992), is used to image the edges of gravity and magnetic anomalies. The ASA is defined as follows:

$$\mathrm{ASA} = \sqrt{G_{xz}^2 + G_{yz}^2 + G_{zz}^2}, \tag{2}$$

where the gradient of the gravity anomaly G_g in the z direction is G_{zz}.

The tilt angle (TA), introduced by Miller and Singh (1994), is defined as the arctangent of the ratio of the vertical gradient to the THG amplitude and constitutes the first balanced interpretation method. The TA is defined as follows:

$$\mathrm{TA} = \mathrm{atan}\left(\frac{G_{zz}}{\sqrt{G_{xz}^2 + G_{yz}^2}}\right). \tag{3}$$

The total horizontal gradient of the TA (THDR) was developed by Verduzco et al. (2004) as an enhanced edge detection filter. The THDR is defined as follows:

$$\mathrm{THDR} = \sqrt{\left(\frac{\partial \mathrm{TA}}{\partial x}\right)^2 + \left(\frac{\partial \mathrm{TA}}{\partial y}\right)^2}. \tag{4}$$

The theta map (TM), introduced by Wijns et al. (2005), is another balanced filter that normalizes the THG by using the ASA. The TM is defined as follows:

$$\mathrm{TM} = \mathrm{acos}\left(\frac{\sqrt{G_{xz}^2 + G_{yz}^2}}{\sqrt{G_{xz}^2 + G_{yz}^2 + G_{zz}^2}}\right). \tag{5}$$

The normalized horizontal tilt angle (TDX) filter, introduced by Cooper and Cowan (2006), utilizes the ratio of the THG amplitude to the absolute value of the vertical gradient. The TDX is defined as follows:

$$\mathrm{TDX} = \mathrm{atan}\left(\frac{\sqrt{G_{xz}^2 + G_{yz}^2}}{|G_{zz}|}\right). \tag{6}$$

The largest eigenvalue (LAMDA) filter, introduced by Sertcelik and Kafadar (2012), is derived from the two-dimensional structural tensor matrix formed by convolving a Gaussian envelope with gradient tensor data. The LAMDA is defined as

$$\begin{bmatrix} T_{11} & T_{12} \\ T_{21} & T_{22} \end{bmatrix} = G_\sigma(x, y) * \begin{bmatrix} G_{xz}^2 & G_{xz}G_{yz} \\ G_{yz}G_{xz} & G_{yz}^2 \end{bmatrix}, \tag{7}$$

where the asterisk ($*$) is the convolution operator, and the Gaussian envelope $G_\sigma(x, y)$ is defined as follows:

$$G_\sigma(x, y) = \frac{1}{2\pi\sigma^2} \mathrm{e}^{-\frac{1}{2}\left(\frac{x^2}{\sigma_x^2} + \frac{y^2}{\sigma_y^2}\right)}, \tag{8}$$

where $\sigma = \sqrt{\sigma_x^2 + \sigma_y^2}$, and in the x and y directions, the standard deviations of $G_\sigma(x, y)$ are σ_x and σ_y, respectively.

$$\mathrm{LAMDA} = \frac{1}{2}\left(T_{11} + T_{22} + \sqrt{(T_{11} - T_{22})^2 + 4T_{12}T_{21}}\right). \tag{9}$$

The tilt angle of the horizontal gradient (TAHG) filter, introduced by Ferreira et al. (2013), is designed to enhance edge detection while avoiding the generation of spurious edges. The TAHG is defined as follows:

$$\mathrm{TAHG} = \operatorname{atan}\left(\frac{\dfrac{\partial \mathrm{THG}}{\partial z}}{\sqrt{\left(\dfrac{\partial \mathrm{THG}}{\partial x}\right)^2 + \left(\dfrac{\partial \mathrm{THG}}{\partial y}\right)^2}}\right). \tag{10}$$

In this study, to reduce noise interference during edge detection, we introduce a Gaussian envelope to the gradient data with reference to Equation (7), whose expression is as follows:

$$\begin{bmatrix} T_{xz} \\ T_{yz} \end{bmatrix} = G_\sigma(x, y) * \begin{bmatrix} G_{xz} \\ G_{yz} \end{bmatrix}. \tag{11}$$

Furthermore, by analogy with the TAHG method presented in Equation (10), we develop a tilt angle method based on the arcsine function under Gaussian envelope constraints for the total gradient modulus (ASTG). Its expression is as follows:

$$\mathrm{ASTG} = \operatorname{asin}\left(\frac{\dfrac{\partial \mathrm{TTHG}}{\partial z}}{\sqrt{\left(\dfrac{\partial \mathrm{TTHG}}{\partial x}\right)^2 + \left(\dfrac{\partial \mathrm{TTHG}}{\partial y}\right)^2 + \left(\dfrac{\partial \mathrm{TTHG}}{\partial z}\right)^2}}\right). \tag{12}$$

In Equation (10), THG (as given by Equation (1)) is the sum of the first-order derivatives of the gravity anomaly in the x and y directions. Similarly, TTHG in Equation (12） is the sum of the derivatives in the x and y directions after introducing a Gaussian envelope. Specifically, the expression for TTHG is given by

$$\mathrm{TTHG} = \sqrt{T_{xz}^2 + T_{yz}^2}. \tag{13}$$

The ASTG method is developed as an enhancement of the TAHG method. It retains effectiveness similar to TAHG but incorporates a Gaussian envelope to effectively suppress the noise amplification associated with the use of higher order derivatives in TAHG. However, ASTG does not completely overcome the limited resolution in edge detection observed in the original TAHG method. To address this issue, we introduce the TANH function into the ASTG framework. Benefiting from its bounded range, strict convergence, and smooth differentiability across the entire domain, the TANH function markedly improves the convergence and sharpness of the boundary response, thereby effectively increasing the resolution of edge detection.

To enhance the resolution of the detection results, we derive the following expression on the basis of the TANH function and the ASTG method:

$$\mathrm{THASTG} = \tanh(\mathrm{ASTG} - k), \tag{14}$$

where tanh denotes the hyperbolic tangent (TANH) function, and k is a positive real number used to adjust the resolution of the detected boundaries.

To evaluate the reliability of Equation (14), we conduct a comparative analysis between the THASTG and other methods described in Section 2 using the synthetic models in Section 3, followed by an application to real gravity data in Section 4. Equation (14) incorporates parameters σ_x, σ_y, and k, whose configurations are discussed in detail in Section 3.2.

3. Synthetic Model Tests

In this section, we evaluate the accuracy of THASTG through synthetic models and compare the edge detection results with those of the THG, ASA, TA, THDR, TM, TDX, LAMDA, and TAHG methods mentioned in Section 2. The synthetic model constructed in this section consists of eight prisms, including three prisms (A, B, and C) of identical size but varying depths; two thin-slab prisms (D and E) with identical widths and heights; and three prisms (F, G, and H) sharing the same central coordinates (Figure 1). The detailed dimensional parameters of the model are provided in Table 1.

To approximate real-world conditions as closely as possible, we design three scenarios, as detailed in Table 2:

(1) The synthetic model contains exclusively positive density contrasts.

(2) The synthetic model incorporates both positive and negative density contrasts.

(3) Random noise equivalent to 5% of the maximum amplitude of the potential field data is added to Scenario 2.

3.1 Model Testing

In this section, a comparative analysis is conducted between the THASTG method and other methods under the three aforementioned scenarios. To facilitate comparison, the parameter values for the THASTG method are directly provided here, with a detailed discussion of parameter selection presented in Section 3.2. For Scenario 1, the parameters of THASTG are set as $\sigma_x = \sigma_y = 0.1$ and $k = 2$; for Scenario 2, the parameters are set as $\sigma_x = \sigma_y = 0.1$ and $k = 2$; and for Scenario 3, the parameters are set as $\sigma_x = \sigma_y = 2$ and $k = 2$.

The gravity potential field data generated for Scenario 1 are detailed in Figures 1c–1f, with the data for the other two scenarios being similar and thus not reiterated subsequently. The edge detection results obtained by the different methods are shown in Figure 2, and the profile results along the section line in Figure 1 are presented in Figure 3. The THG method (Figure 2a) performs well in detecting the boundaries of shallower prisms (A, B, D, and E), but its effectiveness decreases for deeper prisms. As the depth increases, the THG results become more dispersed than the true boundaries (Figure 3a), although the true boundaries align well with the peak values of the THG amplitude. The ASA method (Figure 2b) shows good performance in detecting the boundaries of shallow prisms A and D but appears blurred for other prism boundaries. As the depth increases, the ASA results become increasingly dispersed (Figure 3b) and deviate from the true positions. The TA method (Figure 2c) can simultaneously display the boundaries of prisms at different depths, but it is difficult to directly derive the boundaries from the results (Figure 3c). The THDR method (Figure 2d) performs well in identifying prisms A and D but largely fails to outline the boundaries of deeper prisms. As shown in Figure 3d, THDR offers high resolution, with the results aligning well with the true boundary positions and exhibiting minimal dispersion, although spurious boundaries appear in the detection results. Both the TM (Figure 2e) and TDX (Figure 2f) methods can also simultaneously identify the locations of prisms at different depths, with the former defining prism boundaries

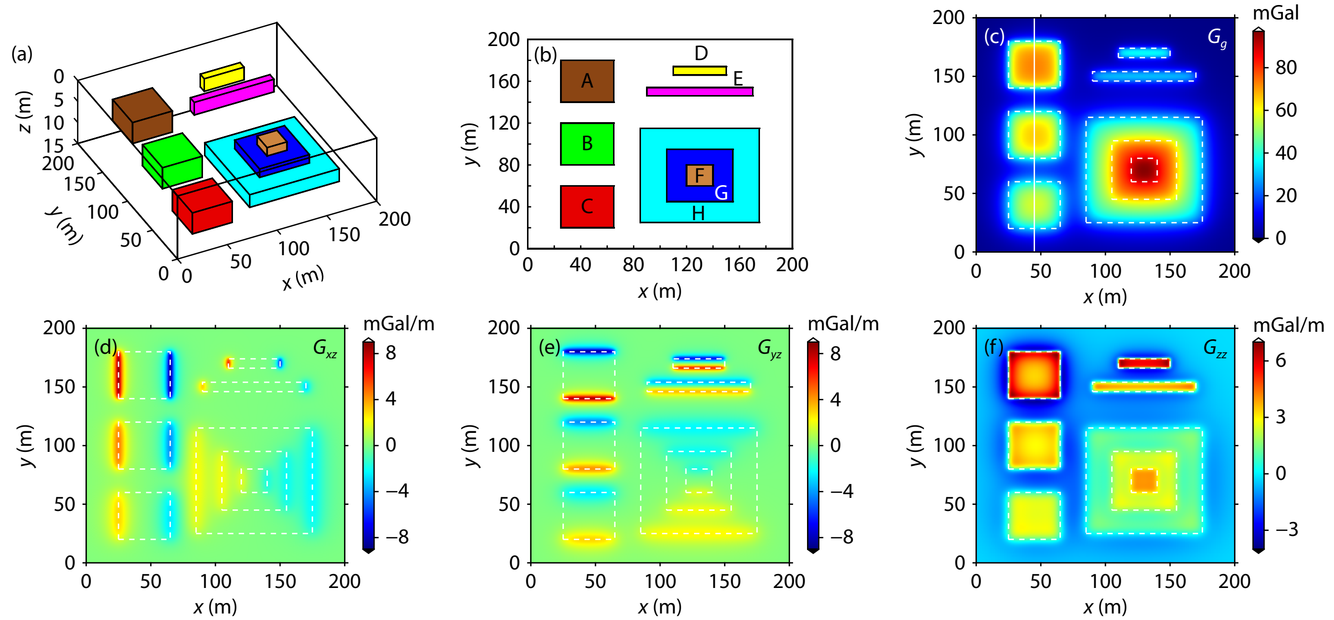

Figure 1. Visualization and geophysical responses of the synthetic models. The solid white line corresponds to the profile path. The dashed white lines represent the actual horizontal positions of the prisms. (a) 3D view. (b) Plan view. (c) Gravity anomaly G_g generated by Scenario 1. (d) Gravity horizontal gradient anomaly G_{xz} generated by Scenario 1. (e) Gravity horizontal gradient anomaly G_{yz} generated by Scenario 1. (f) Gravity vertical gradient anomaly G_{zz} generated by Scenario 1.

Table 1. Parameters of the synthetic model.

Parameter/model label	A	B	C	D	E	F	G	H
x-coordinates of center (m)	45	45	45	130	130	130	130	130
y-coordinates of center (m)	160	100	40	170	150	70	70	70
z-coordinates of center (m)	3.5	6	8.5	2.5	4	5	7	9
Length (m)	40	40	40	40	80	20	50	90
Width (m)	40	40	40	8	8	20	50	90
Height (m)	5	5	5	3	3	2	2	3

Table 2. Parameters of the synthetic model for the three scenarios.

Scenario	Noise	Density (g/cm^3)							
		A	B	C	D	E	F	G	H
1	No	0.2	0.2	0.2	0.21	0.21	0.15	0.23	0.25
2	No	0.2	−0.2	0.2	0.21	−0.21	0.15	0.23	0.25
3	Yes	0.2	−0.2	0.2	0.21	−0.21	0.15	0.23	0.25

using minimum values and the latter using maximum values. However, as depth increases, the agreement between their results and the true boundary positions deteriorates (Figures 3e–3f), with the latter exhibiting higher resolution. The LAMDA method (Figure 2g) performs well in identifying prisms A and D, with results aligning accurately with the true boundary positions and yielding smoother information on the map (Figure 3g). The TAHG method (Figure 2h) defines the boundaries of prisms at different depths using maximum values, and the results match well with the true boundary positions, but spurious boundaries interfere between the prisms (Figure 3h). The THASTG method (Figure 2i) also defines the boundaries of prisms at different depths using maximum values, significantly enhancing the resolution of the detection results without introducing spurious boundaries (Figure 3i).

The edge detection results obtained by the different methods under Scenario 2 are detailed in Figure 4, and the profile results along the section line in Figure 1 are presented in Figure 5. The THG method (Figure 4a) effectively identifies the boundaries of shallower prisms (A, B, D, and E), whereas the ASA (Figure 4b), THDR (Figure 4d), and LAMDA (Figure 4g) methods perform well in detecting shallow prisms A and D. However, for deeper prisms, THG, ASA, THDR, and LAMDA exhibit limited detection capabilities. As depth increases, the THG (Figure 5a), ASA (Figure 5b),

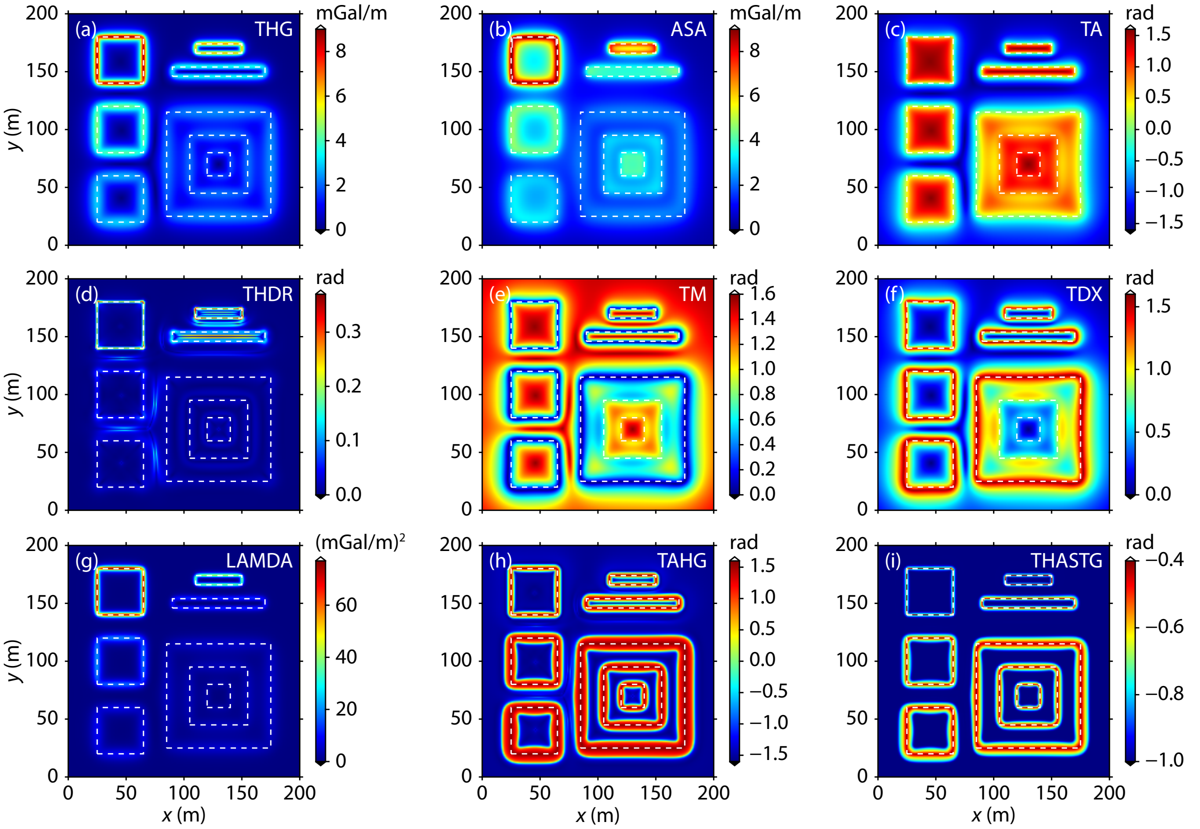

Figure 2. Edge detection results for the different methods for Scenario 1. (a) THG. (b) ASA. (c) TA. (d) THDR. (e) TM. (f) TDX. (g) LAMDA, with $\sigma_x = \sigma_y = 0.1$. (h) TAHG. (i) THASTG, with $\sigma_x = \sigma_y = 0.1$ and $k = 2$.

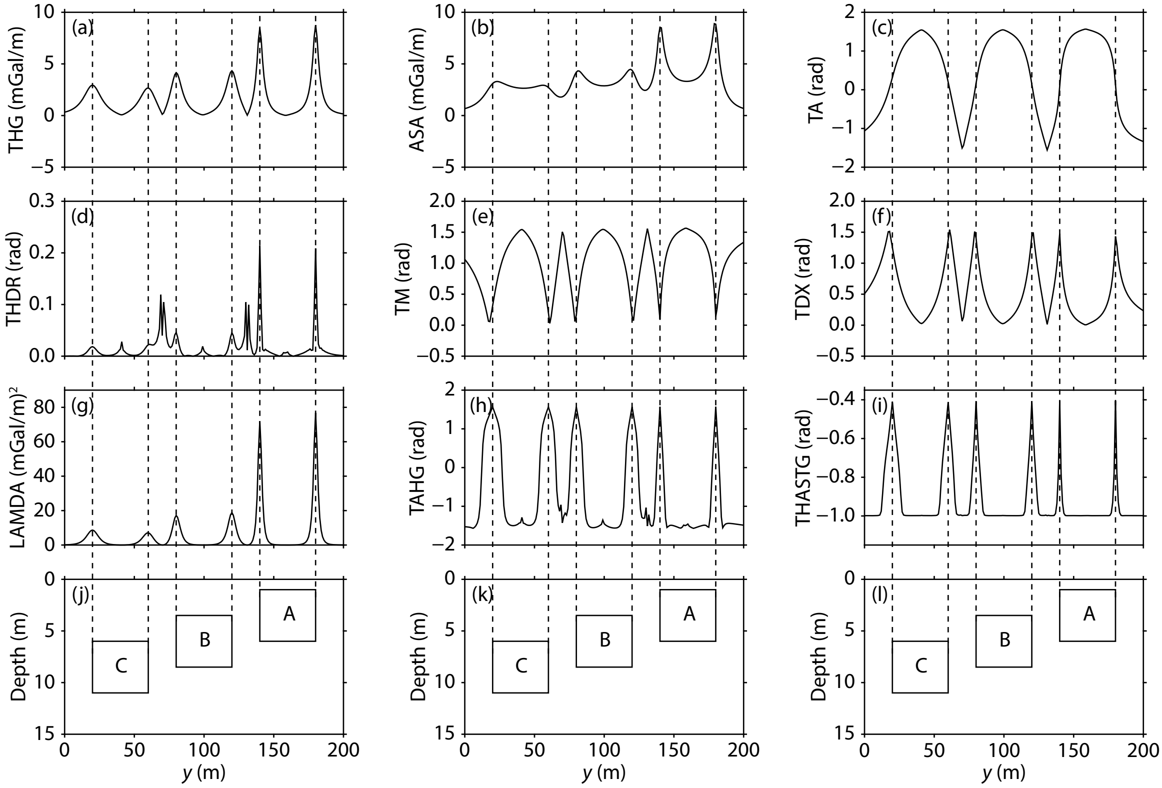

Figure 3. Profile results for the different methods for Scenario 1. The dashed black lines indicate the true boundary positions of the prisms. (a) THG. (b) ASA. (c) TA. (d) THDR. (e) TM. (f) TDX. (g) LAMDA, with $\sigma_x = \sigma_y = 0.1$. (h) TAHG. (i) THASTG, with $\sigma_x = \sigma_y = 0.1$ and $k = 2$. (j–l) Cross-sections of the prisms.

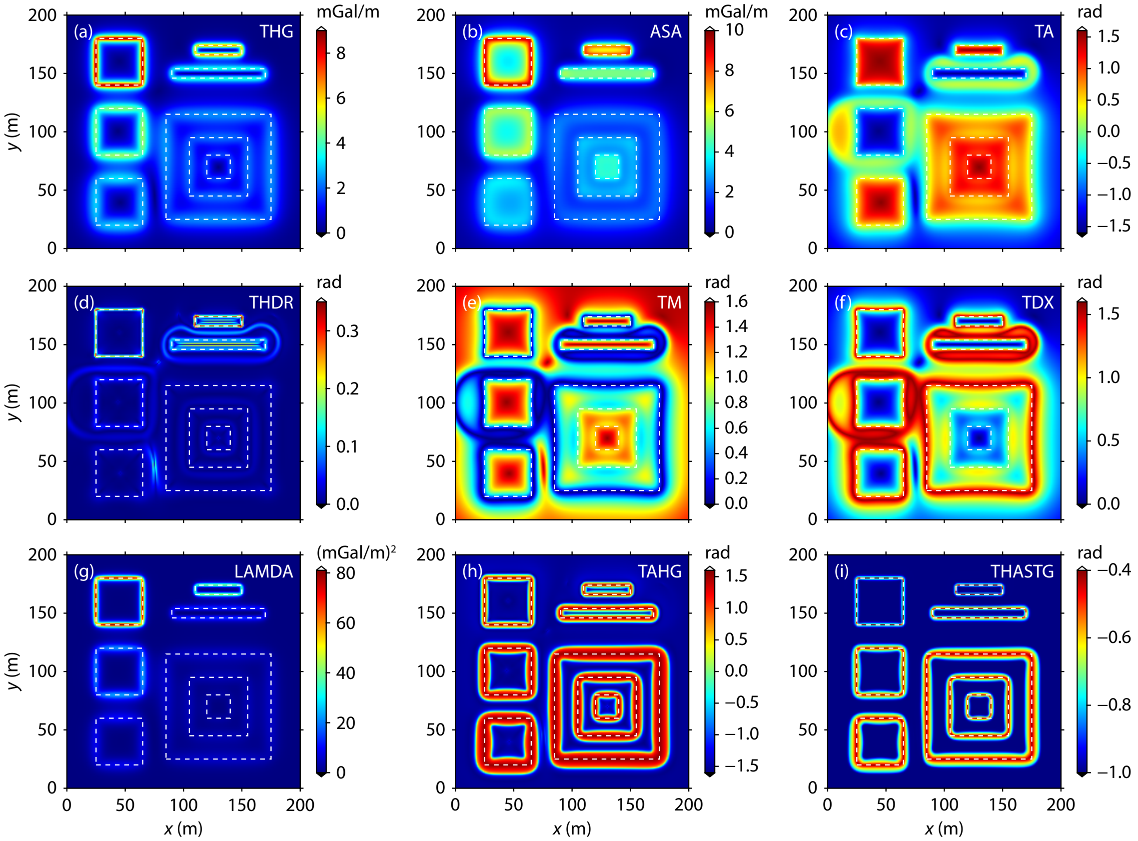

Figure 4. Edge detection results for the different methods for Scenario 2. (a) THG. (b) ASA. (c) TA. (d) THDR. (e) TM. (f) TDX. (g) LAMDA, with $\sigma_x = \sigma_y = 0.1$. (h) TAHG. (i) THASTG, with $\sigma_x = \sigma_y = 0.1$ and $k = 2$.

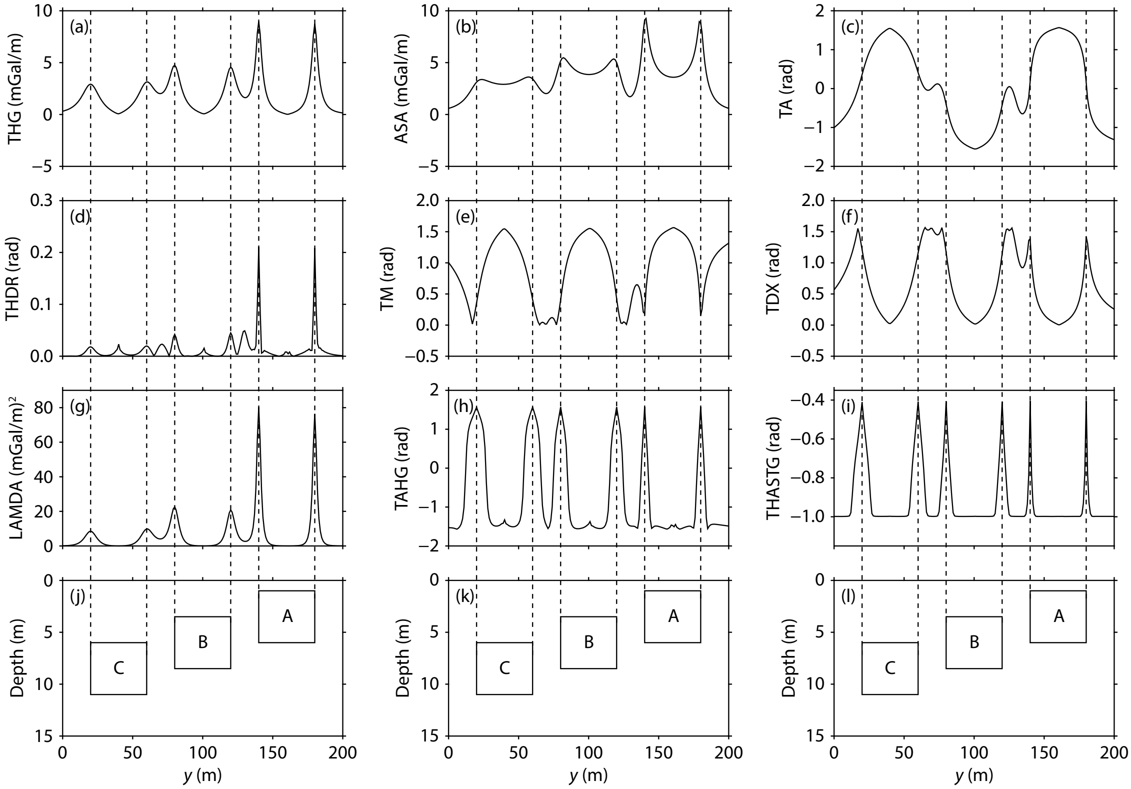

Figure 5. Profile results for the different methods for Scenario 2. The dashed black lines indicate the true boundary positions of the prisms. (a) THG. (b) ASA. (c) TA. (d) THDR. (e) TM. (f) TDX. (g) LAMDA, with $\sigma_x = \sigma_y = 0.1$. (h) TAHG. (i) THASTG, with $\sigma_x = \sigma_y = 0.1$ and $k = 2$. (j–l) Cross-sections of the prisms.

THDR (Figure 5d), and LAMDA (Figure 5g) results become increasingly dispersed. Although the results of THG, THDR, and LAMDA maintain good alignment with the true boundaries, those of ASA gradually deviate from the actual boundary positions, and spurious interference appears in the THDR results. The TA (Figure 4c), TM (Figure 4e), and TDX (Figure 4f) methods simultaneously capture the boundaries of prisms at different depths but introduce false boundary information. In Figure 5, the TA method (Figure 5c) clearly fails to visually represent the prism boundaries. As the prism depth increases, the TM (Figure 5e) and TDX (Figure 5f) results progressively decrease in agreement with the true boundaries. Both the TAHG (Figure 4h) and THASTG (Figure 4i) methods define the boundaries of prisms at different depths using maximum values, and their results (Figure 5h and Figure 5i, respectively) demonstrate higher resolution than those of the other methods (Figures 5a–5g). However, compared with TAHG, THASTG not only provides higher resolution but also effectively suppresses spurious signals during detection.

The edge detection results obtained by the different methods under Scenario 3 are detailed in Figure 6, and the profile results along the section line in Figure 1 are presented in Figure 7. The THG (Figure 6a), ASA (Figure 6b), and LAMDA (Figure 6g) methods yield results largely consistent with those from the previous two scenarios, showing minimal susceptibility to noise interference. However, the graphical outputs of THG (Figure 7a) and ASA (Figure 7b) display slight fluctuations, whereas the results of LAMDA (Figure 7g) appear smoother because of its built-in Gaussian envelope. The THDR (Figure 6d) and TAHG (Figure 6h) methods have difficulty clearly distinguishing prism boundary positions, with the profile results in Figure 7d and Figure 7h showing predominantly anomalous signal fluctuations, indicating significant susceptibility to noise interference. The TA (Figure 6c), TM (Figure 6e), and TDX (Figure 6f) methods remain capable of simultaneously identifying the boundaries of prisms at different depths; however, the profile results in Figure 7c, Figure 7e, and Figure 7f exhibit anomalous amplitude fluctuations, indicating that these methods are also prone to noise interference and introduce false boundary information. The results of THASTG (Figure 6i and Figure 7i) are essentially consistent with those from the previous two scenarios, as THASTG not only simultaneously identifies boundaries of prisms at varying depths but also delivers high resolution, excellent convergence, minimal susceptibility to noise interference during detection, and no spurious boundaries.

3.2 Parameter Settings

This section provides a detailed evaluation of the parameters σ_x, σ_y, and k in the THASTG method using the aforementioned

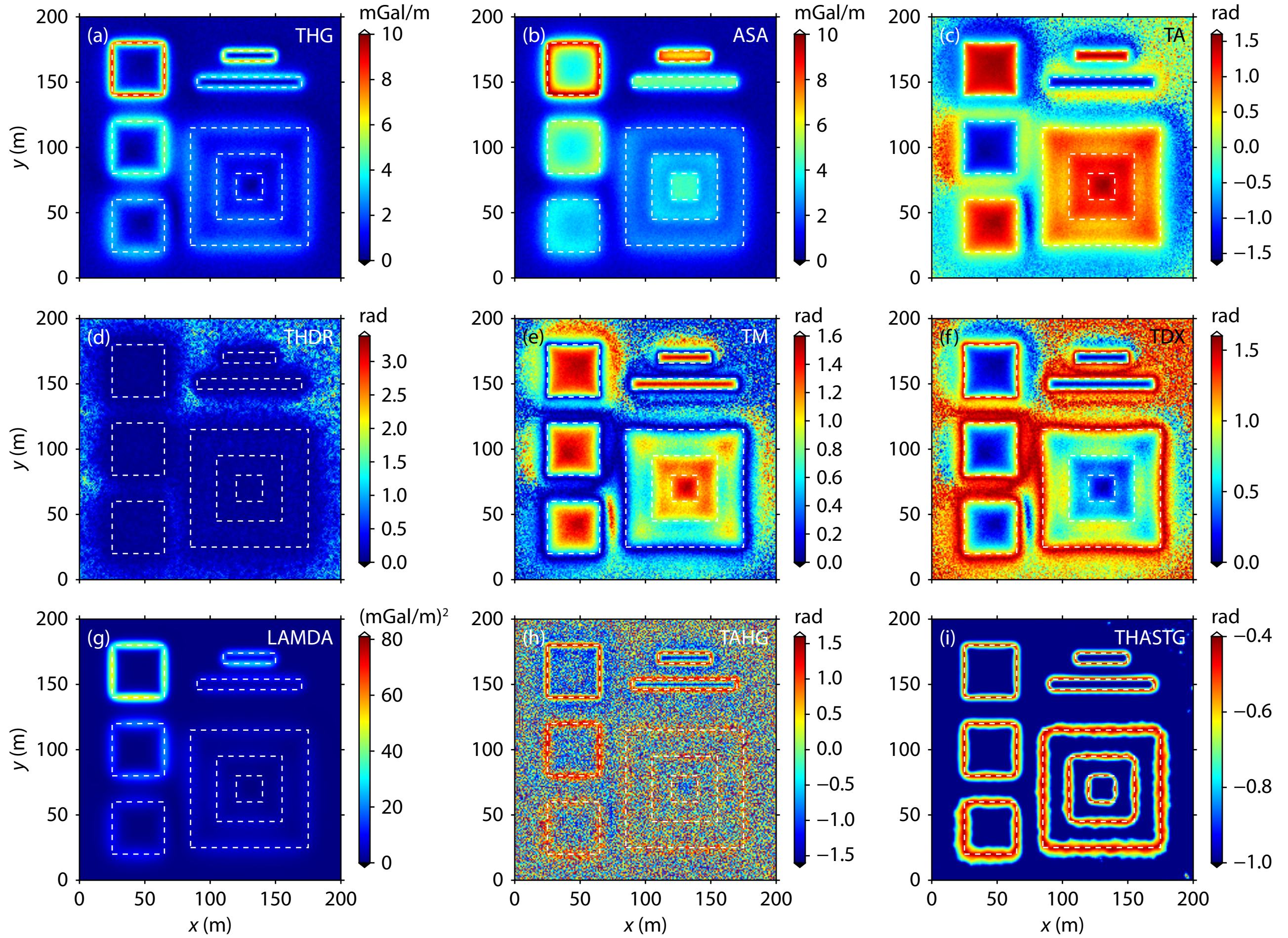

Figure 6. Edge detection results for the different methods for Scenario 3. (a) THG. (b) ASA. (c) TA. (d) THDR. (e) TM. (f) TDX. (g) LAMDA, with $\sigma_x = \sigma_y = 2$. (h) TAHG. (i) THASTG, with $\sigma_x = \sigma_y = 2$ and $k = 2$.

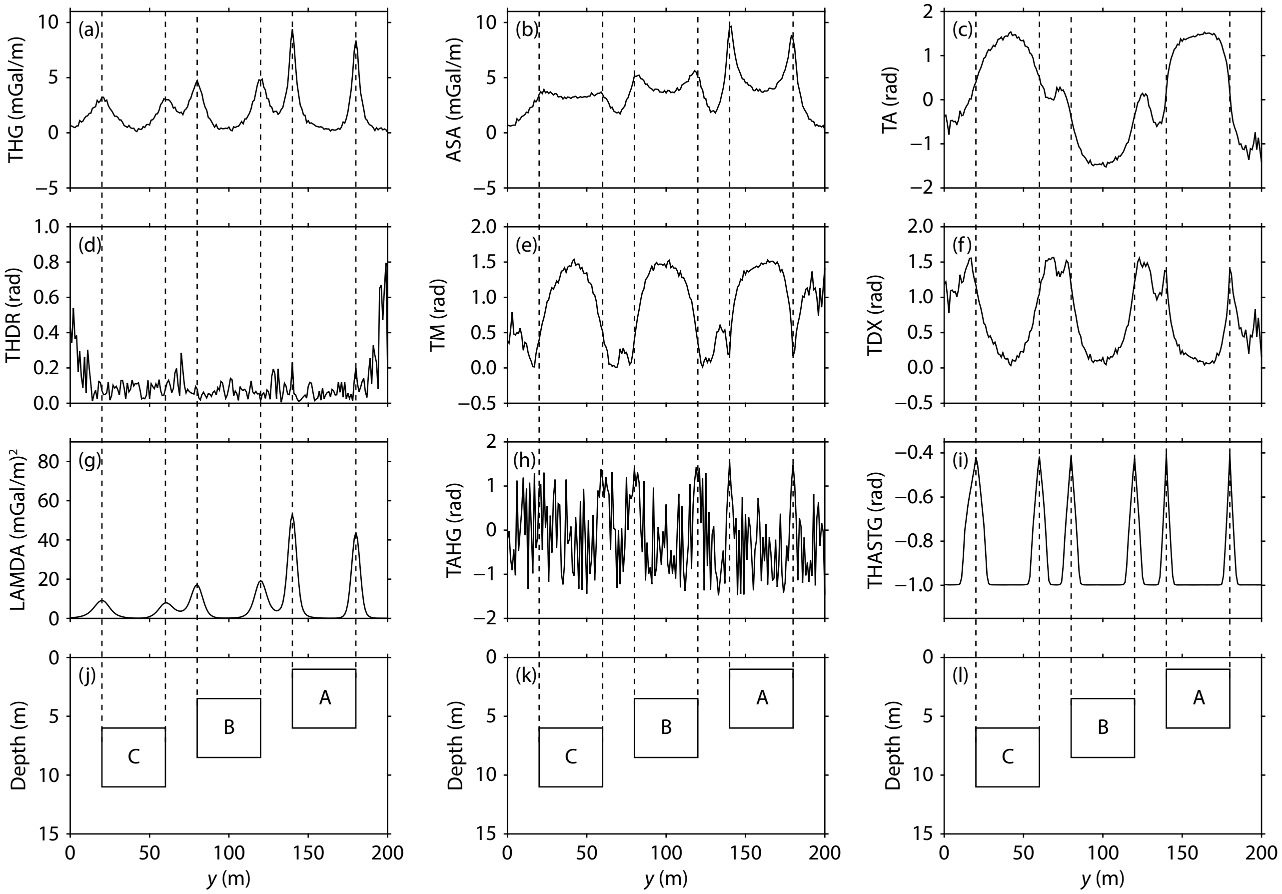

Figure 7. Profile results for the different methods for Scenario 3. The dashed black lines indicate the true boundary positions of the prisms. (a) THG. (b) ASA. (c) TA. (d) THDR. (e) TM. (f) TDX. (g) LAMDA, with $\sigma_x = \sigma_y = 2$. (h) TAHG. (i) THASTG, with $\sigma_x = \sigma_y = 2$ and $k = 2$. (j–l) Cross-sections of the prisms.

synthetic models and three different scenarios. Specifically, the parameter k is first fixed while modifying parameters σ_x and σ_y to analyze their effects on the detection results. The parameters σ_x and σ_y are subsequently fixed while modifying parameter k to analyze its influence on the detection outcomes.

In the parameter sensitivity analysis, the Gaussian envelope parameter controls the cutoff wavelength of the low-pass filter. Its value directly affects the balance between suppressing high-frequency noise and retaining effective structural signals. Following previous studies (Xue ZX et al., 2025a), the Gaussian envelope parameter is tested here with values of 0.1, 0.5, 1, and 2. The parameter k is used to shift the ASTG signal numerically so that it falls within the interval where the TANH function exhibits the most pronounced nonlinear response, which favors boundary convergence. In this study, k is set to 0.5, 1, 2, and 5 for a systematic investigation of its influence. The following sections examine the effects of these two parameters under different values on boundary detection performance and determine their appropriate settings.

The parameter k is first fixed at 2, whereas parameters σ_x and σ_y are sequentially set to 0.1, 0.5, 2, and 5. The influence of variations in σ_x and σ_y on the THASTG method is then analyzed under the three different scenarios. The edge detection results obtained by THASTG under each scenario are detailed in Figure 8, and the corresponding profile results along the section line in Figure 1 are shown in Figure 9. Figure 8 demonstrates that the THASTG method effectively balances the amplitudes of the prisms at different depths, regardless of the specific values chosen for parameters σ_x and σ_y. However, as shown in Figures 8a–8h, as the values of σ_x and σ_y increase, the detection results of THASTG become more dispersed compared to the true boundaries. When $\sigma_x = \sigma_y = 5$, Figures 8d and 8h show partial loss of boundary signals for overlapping prisms. Figures 9a–9h indicate that when $\sigma_x = \sigma_y = 0.1$, the results exhibit higher resolution. However, when $\sigma_x = \sigma_y = 5$, spurious boundary information begins to appear in Figure 9h. This result suggests that under both the first and second scenarios, THASTG achieves better detection performance when $\sigma_x = \sigma_y = 0.1$ and $k = 2$. In the third scenario, however, Figures 8i–8j fail to directly reveal the model boundaries, and Figure 8l, similar to Figures 8d and 8h, shows partial loss of boundary signals for overlapping prisms. Furthermore, Figures 9i–9j are dominated by irregular noise interference, whereas Figures 9k–9l are generally consistent with the results from both the first and second scenarios. Nevertheless, as the values of σ_x and σ_y increase, the resolution of the THASTG results decreases, and the outputs become more dispersed relative to the true boundaries. This finding indicates that in the presence of noise, appropriate values of σ_x and σ_y must be selected to ensure high resolution of the final detection results. Specifically, under the third scenario, THASTG performs optimally when $\sigma_x = \sigma_y = 2$ and

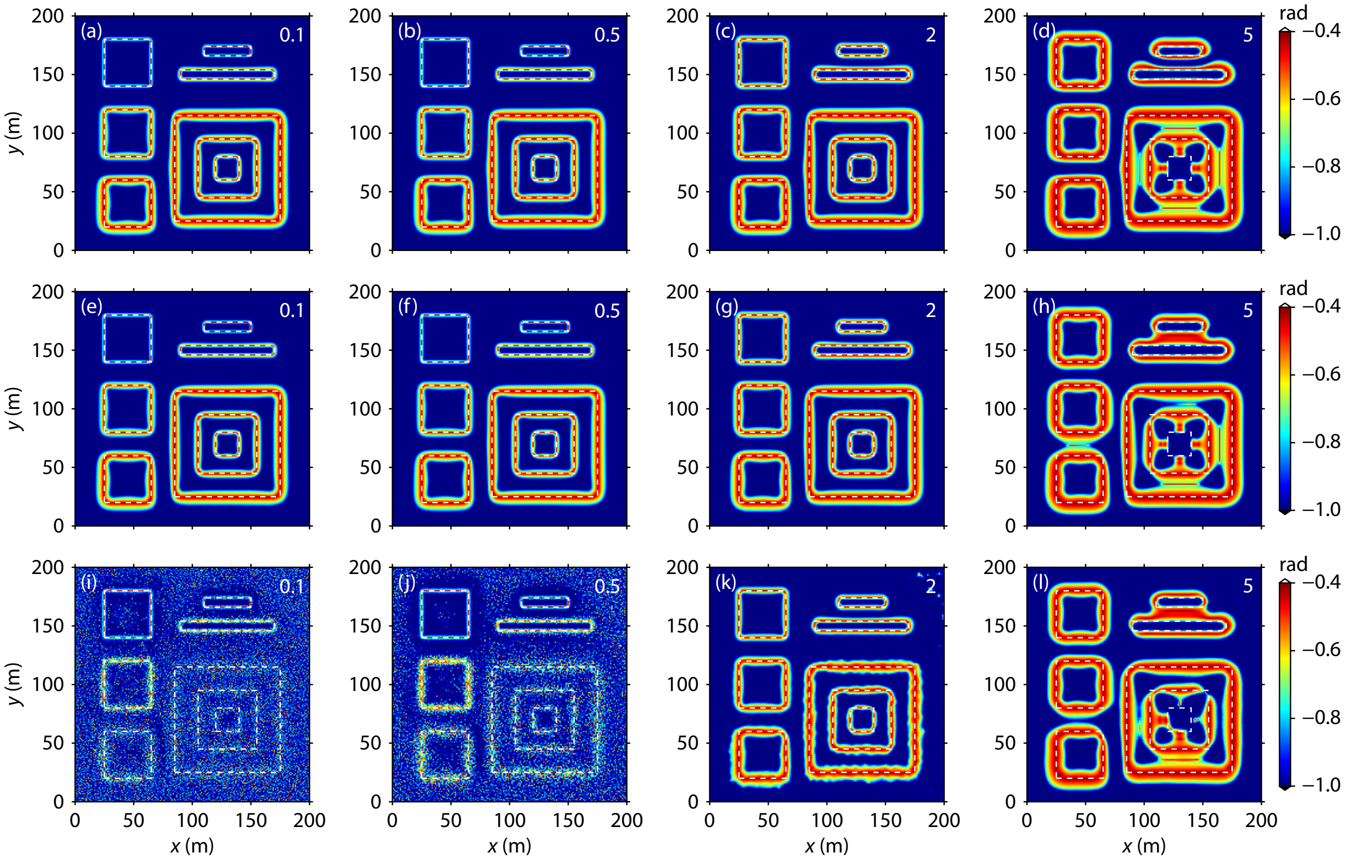

Figure 8. Effects of Gaussian envelope parameter variations in different scenarios (a–d: Scenario 1; e–h: Scenario 2; i–l: Scenario 3; a–l: $k = 2$). (a, e, i) THASTG, with $\sigma_x = \sigma_y = 0.1$. (b, f, j) THASTG, with $\sigma_x = \sigma_y = 0.5$. (c, g, k) THASTG, with $\sigma_x = \sigma_y = 2$. (d, h, l) THASTG, with $\sigma_x = \sigma_y = 5$.

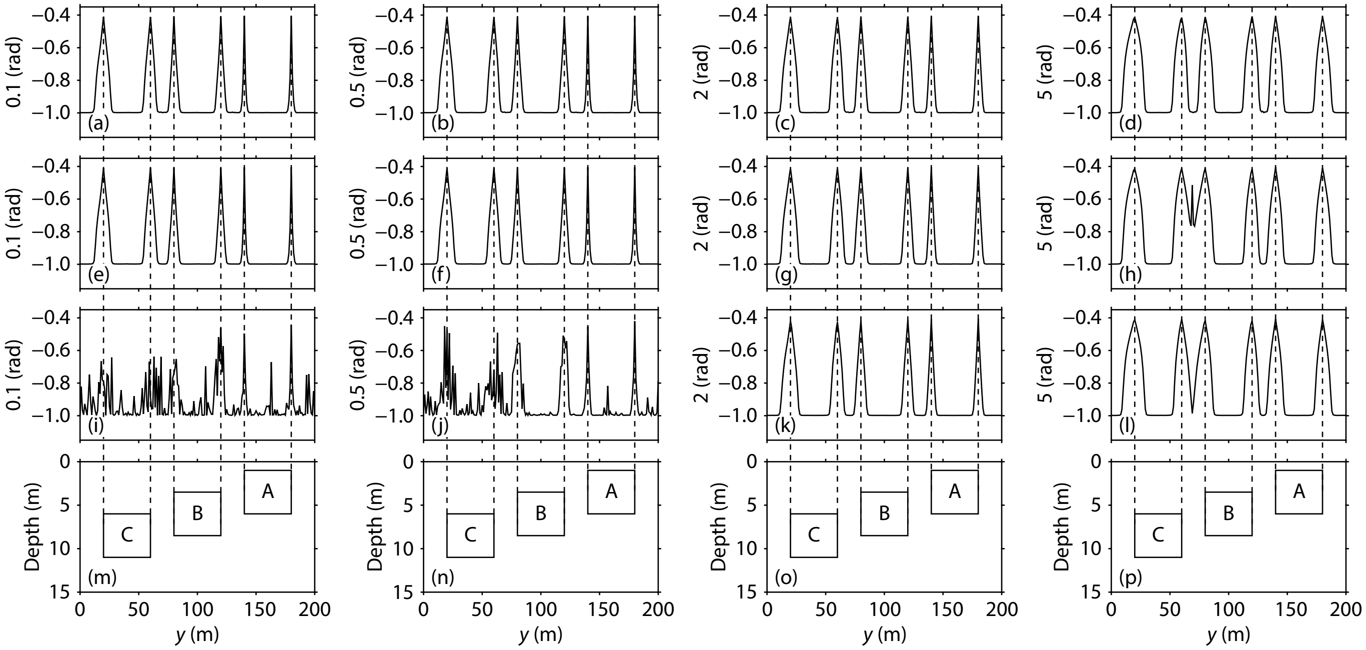

Figure 9. Profiles of Gaussian envelope parameter variations in different scenarios (a–d: Scenario 1; e–h: Scenario 2; i–l: Scenario 3; a–l: $k = 2$). (a, e, i) THASTG, with $\sigma_x = \sigma_y = 0.1$. (b, f, j) THASTG, with $\sigma_x = \sigma_y = 0.5$. (c, g, k) THASTG, with $\sigma_x = \sigma_y = 2$. (d, h, l) THASTG, with $\sigma_x = \sigma_y = 5$. (m–p) Cross-sections of the prisms.

$k = 2$.

The observed behavior stems from the core physical role of the Gaussian envelope parameter: It acts as a scale-controlling factor for low-pass filtering. An increase in its value implies stronger spatial smoothing. Although this can suppress high-frequency noise, it also attenuates the high-frequency signals that characterize boundaries, leading to a broadening of the boundary response and a reduction in peak amplitude, which manifests as a "smearing" of the results. Therefore, the selection of this parameter represents a trade-off between boundary resolution and noise resistance. A smaller value (e.g., 0.1) favors higher resolution but increases sensitivity to noise, whereas a larger value (e.g., 5) enhances smoothing at the cost of reduced resolving power.

On the basis of the aforementioned parameter evaluation, parameters σ_x and σ_y are fixed at 0.1 for both the first scenario and the second scenario and at 2 for the third scenario, whereas parameter k is sequentially set to 0.5, 1, 2, and 5. The edge detection results obtained by the THASTG method under these parameter configurations are shown in Figure 10, with the corresponding profile results along the section line in Figure 1 presented in Figure 11. As shown in Figure 10, as the value of parameter k increases, the detection results become increasingly convergent, indicating near-perfect alignment with the true boundaries. Figure 11 indicates that under all three scenarios, the resolution of the THASTG results progressively improves with increasing values of parameter k. However, significant signal fluctuations are observed between prisms A, B, and C when k = 0.5, 1, and 5. These fluctuations are effectively suppressed when k = 2. Consequently, larger values of k do not always yield better performance, and an appropriate value must be selected for optimal computational results. For the three scenarios examined here, $k = 2$ proves to be the most suitable choice.

The parameter k essentially modulates the response interval of the ASTG signal within the TANH function. Increasing k shifts the entire signal negatively, causing it to enter the saturation region of TANH more rapidly, thereby leading to a more convergent boundary response. However, if k is too small (e.g., 0.5), the signal remains in the gently varying region of the function, resulting in oscillatory artifacts. Conversely, an excessively large k (e.g., 5) overdrives the signal into deep saturation, which suppresses meaningful detail. The choice of $k = 2$ places the signal within the most nonlinear transition zone of TANH, achieving an optimal balance between interference suppression and detail preservation. Therefore, for both the first and second scenarios, the optimal parameter configuration for the THASTG method is $\sigma_x = \sigma_y = 0.1$ and $k = 2$, whereas for the third scenario, the optimal parameter configuration remains $\sigma_x = \sigma_y = 2$ and $k = 2$.

The parameters described above serve as fundamental guidelines

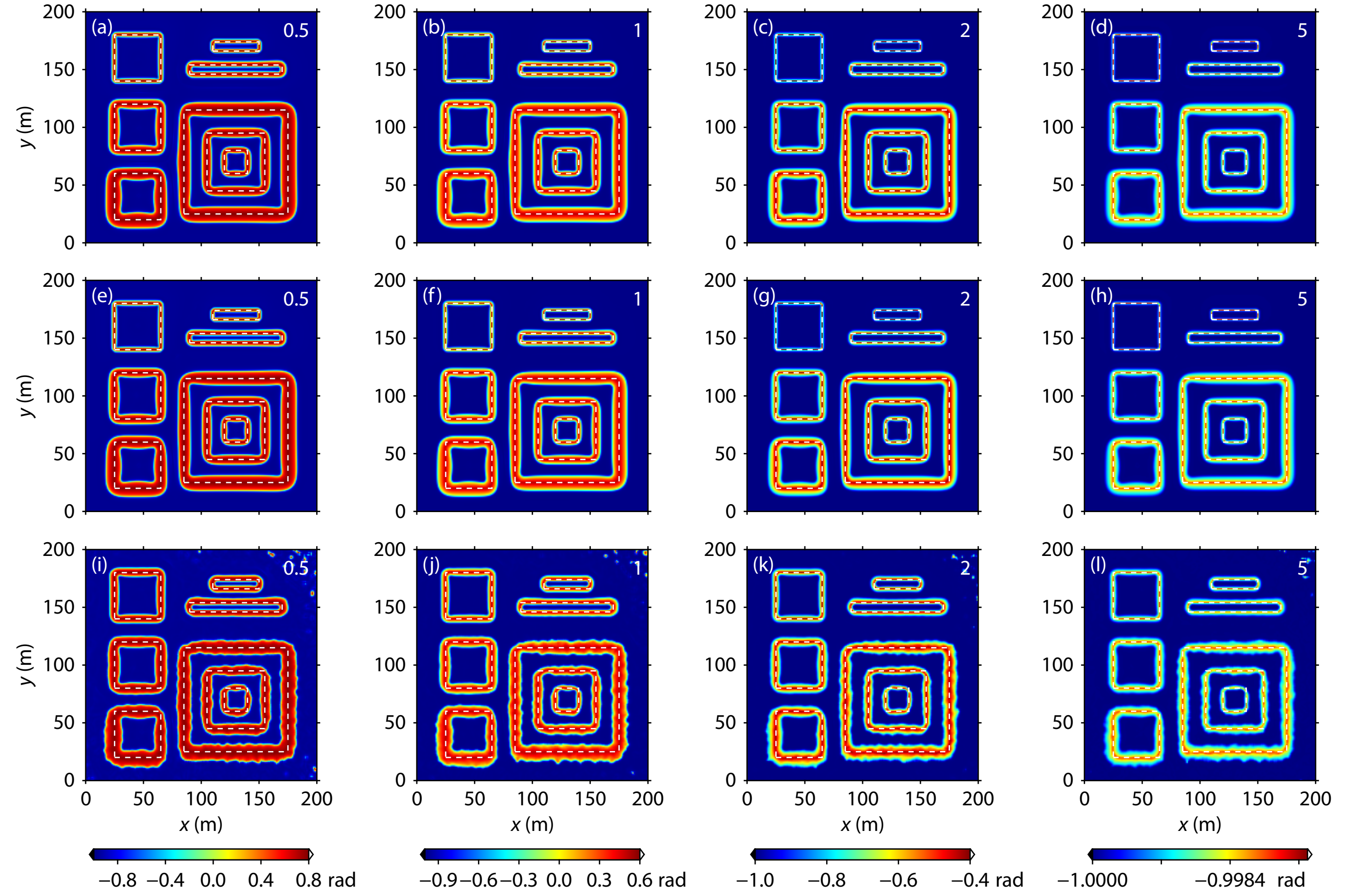

Figure 10. Effects of k parameter variations in different scenarios (a–d: Scenario 1, with $\sigma_x = \sigma_y = 0.1$; e–h: Scenario 2, with $\sigma_x = \sigma_y = 0.1$; i–l: Scenario 3, with $\sigma_x = \sigma_y = 2$). (a, e, i) THASTG, with $k = 0.5$. (b, f, j) THASTG, with $k = 1$. (c, g, k) THASTG, with $k = 2$. (d, h, l) THASTG, with $k = 5$.

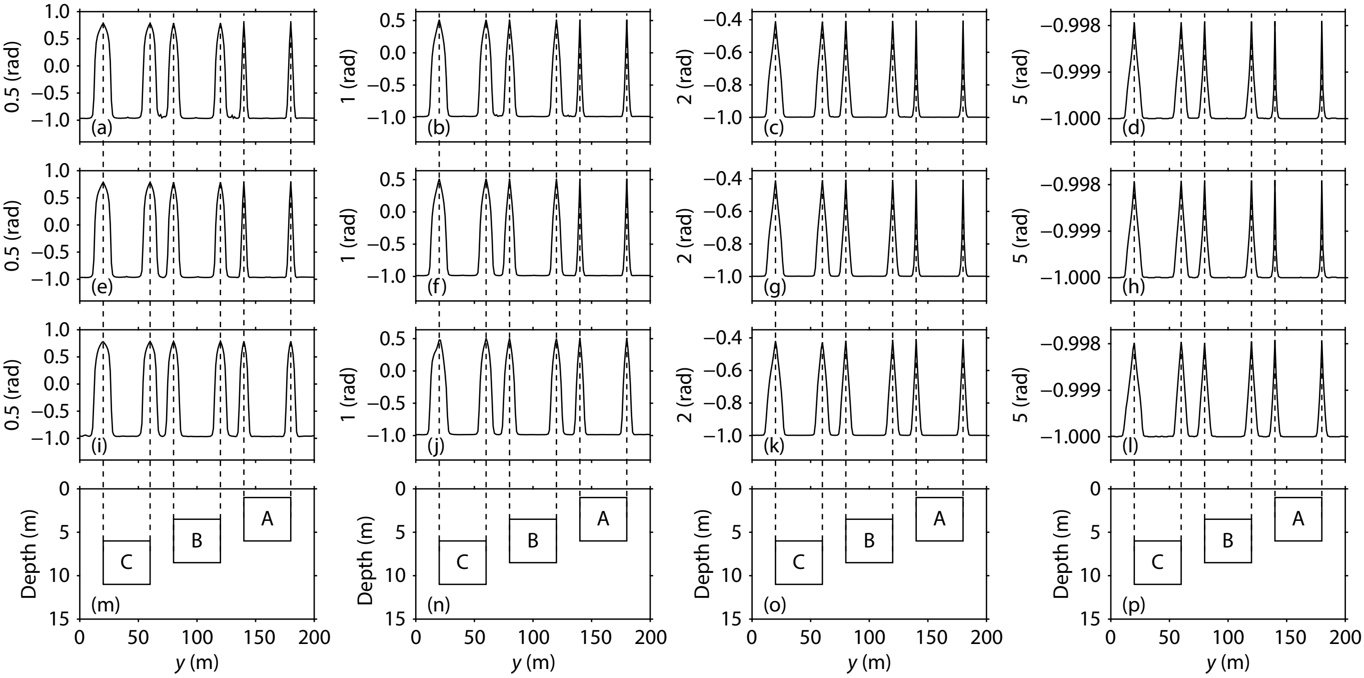

Figure 11. Profiles of *k* parameter variations in different scenarios (a–d: Scenario 1, with $\sigma_x = \sigma_y = 0.1$; e–h: Scenario 2, with $\sigma_x = \sigma_y = 0.1$; i–l: Scenario 3, with $\sigma_x = \sigma_y = 2$). (a, e, i) THASTG, with *k* = 0.5. (b, f, j) THASTG, with *k* = 1. (c, g, k) THASTG, with *k* = 2. (d, h, l) THASTG, with *k* = 5. (m–p) Cross-sections of the prisms.

for applying the method. Specifically, parameters σ_x and σ_y balance the suppression of noise against the resolution of boundary signals. Increasing their values generally improves noise resistance, although excessively high values can lead to the loss of valid signal information. Parameter *k* primarily controls the convergence and stability of the identified boundaries. Appropriately increasing its value yields more convergent results but exceeding a reasonable range may introduce artifacts or cause loss of detail. In practical applications, if significant residual noise remains after data preprocessing, the values of parameters σ_x and σ_y may be increased accordingly (it is recommended that they not exceed 2). To achieve optimal overall performance, a value of *k* = 2 is recommended.

4. Application to Real Data

To evaluate the reliability of the THASTG method in practical applications, this section applies it to satellite gravity anomaly data from the South China Sea.

4.1 Data and Results

Owing to their advantages of easy accessibility, broad coverage, high resolution, and high precision, satellite gravity data have become crucial for studying the internal structure and geodynamic processes of Earth. The South China Sea serves as a natural laboratory for investigating deep dynamic systems in the western Pacific marginal seas, and accurate identification of its tectonic boundaries is fundamental to revealing the region’s formation, evolutionary mechanisms, and geodynamic processes (Hayes and Nissen, 2005; Metcalfe, 2011). To further demonstrate the reliability of the new method, this section applies the THASTG approach to the South China Sea region using satellite gravity data and conducts a detailed comparative analysis with the methods mentioned in Section 2.

The gravity data used in this section are derived from the SGG-UGM-2 combined gravity field model with a resolution of 5′ × 5′. This model integrates data from GOCE (Gravity field and steady-state Ocean Circulation Explorer), GRACE (Gravity Recovery and Climate Experiment), satellite altimetry, and the EGM2008 (Earth Gravitational Model 2008) model, achieving overall accuracy comparable to other models (e.g., EIGEN-6C4) while demonstrating significantly higher accuracy in the China region than EGM2008 (Liang W et al., 2020; Ariff et al., 2021). The Bouguer gravity anomaly data for the South China Sea region are first computed via the International Centre for Global Earth Models (ICGEM) website (https://icgem.gfz-potsdam.de/home), followed by the application of a Gaussian filter to mitigate the inevitable noise effects in satellite gravity data. After multiple trials, the Gaussian filter employs a Mapinfo-built function with a 9 × 9 kernel and σ = 1. The Bouguer gravity anomaly after Gaussian filtering is detailed in Figure 12a, whereas the edge detection results for the South China Sea region obtained by different methods are presented in Figures 12b–12j. Figure 12h corresponds to the result of the LAMDA method using the parameter set $\sigma_x = \sigma_y = 1$, and Figure 12j corresponds to the result of the THASTG method configured with parameters $\sigma_x = \sigma_y = 1$, $k = 2$.

The complex Bouguer gravity anomalies in the South China Sea region, characterized by alternating positive and negative anomalies, are shown in Figure 12a. Areas such as the Central Basin, the Sulu Sea, and the Celebes Sea exhibit relatively high Bouguer gravity anomaly values. From the Central Basin toward the marginal seas and continental shelf, the Bouguer gravity anomalies gradually decrease. Pronounced gravity anomaly gradient zones

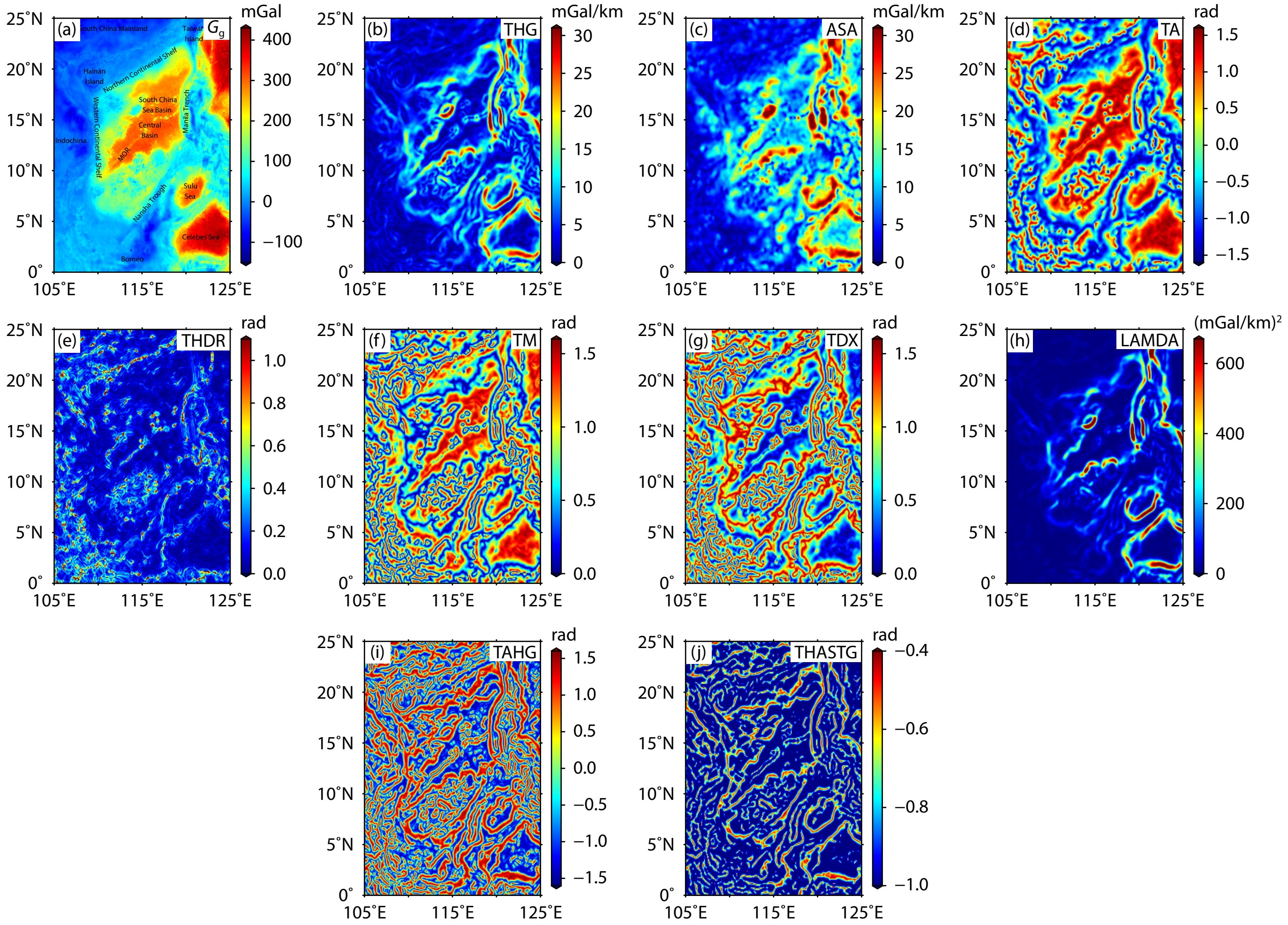

Figure 12. (a) Gaussian-filtered gravity anomaly data for the South China Sea. MOR: Mid-ocean ridge of the Central Basin. (b) THG. (c) ASA. (d) TA. (e) THDR. (f) TM. (g) TDX. (h) LAMDA, with $\sigma_x = \sigma_y = 1$. (i) TAHG. (j) THASTG, with $\sigma_x = \sigma_y = 1$ and $k = 2$.

are developed around the periphery of the South China Sea Basin. The results from the THG (Figure 12b), ASA (Figure 12c), THDR (Figure 12e), and LAMDA (Figure 12h) methods are dominated by large-amplitude signals in regions such as the Central Basin, Sulu Sea, and Sulawesi Sea, whereas the tectonic boundaries in the northwestern and southern parts of the South China Sea Basin appear blurred. Although TA (Figure 12d), TM (Figure 12f), and TDX (Figure 12g) effectively balance amplitude signals of varying magnitudes, TA fails to provide clear tectonic boundaries directly, and all three methods inevitably introduce spurious boundaries. Their results are largely interconnected, making it difficult to extract authentic boundary information. For instance, TA, TM, and TDX depict the northeastern margin of the mid-ocean ridge as several clustered spot-like structures, which deviates from the actual situation. Compared with the other methods, TAHG (Figure 12i) and THASTG (Figure 12j) yield more effective detection results in the South China Sea. Although delineating boundaries in regions with large-amplitude signals, such as the Central Basin, Sulu Sea, and Sulawesi Sea, they also clearly reveal tectonic boundaries in areas with weak-amplitude signals, such as the northwestern and southern parts of the South China Sea Basin. However, compared with TAHG, THASTG produces more convergent results with higher resolution, effectively suppressing scattered spot-like signal interference and providing clearer and more definitive information on the map. Therefore, compared with other conventional methods, the THASTG method can delineate tectonic boundaries in the South China Sea region with higher resolution and greater clarity.

4.2 Discussion

Figure 12a shows an integrated compilation of multi-source fault data derived from seismic data, gravity data, active fault mapping projects, active fault prospecting, and information provided by the China Seismic Active Fault Survey Data Center (Hu SX et al., 2021; Guo DM and Xue ZX, 2023; Wu et al., 2024; Xue ZX et al., 2025b). The precise planar locations of faults in the South China Sea region extracted using the THASTG method are shown in Figure 13b. The results demonstrate that THASTG directly identifies fault positions through maximum values with high localization accuracy, effectively suppresses noise interference, and does not produce spurious boundaries. A comprehensive comparison between Figures 13a and 13b demonstrates a high degree of consistency in the overall orientation and spatial distribution of the fault structures revealed in both. Specifically, the faults identified by the THASTG method in Figure 13b correspond well with the integrated multi-source fault data compiled in Figure 13a,

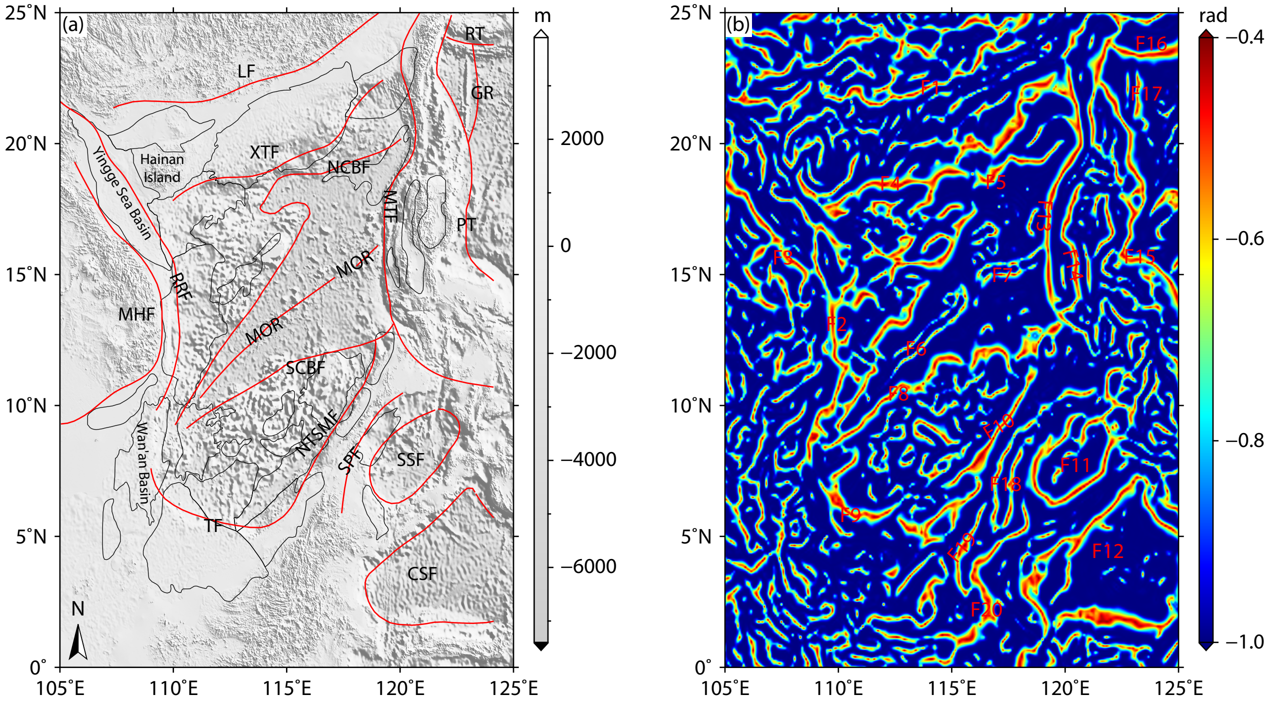

Figure 13. (a) Terrain and tectonic setting of the South China Sea and its surrounding areas, with terrain data from ETOPO1 (Amante and Eakins 2009). The integrated compilation of multi-source fault data is listed here (Hu SX et al., 2021; Guo DM and Xue ZX, 2023; Wu et al., 2024; Xue ZX et al., 2025b; and China Seismic Active Fault Survey Data Center). LF: Littoral Fault; RRF: Red River Fault; MHF: Majiang–Heishuihe Fault; XTF: Xisha Trough Fault; NCBF: Northern Central Basin Fault; SCBF: Southern Central Basin Fault; MOR: mid-ocean ridge of the Central Basin; TF: Tingjia Fault; NTSMF: Southeastern Margin Fault Zone of the Nansha Trough; SSF: Sulu Sea Fault Zone; CSF: Celebes Sea Fault Zone; SPF: Sabah–Palawan Fault Zone; MTF: Manila Trench Fault; PT: Philippine Trench; GR: Gagua Ridge; RT: Ryukyu Trench; (b) Edge detection results of the THASTG method.

further validating the reliability and effectiveness of the proposed method. On this basis, a total of 20 major faults are interpreted in this study, namely the Littoral Fault Zone (F1), Red River Fault Zone (F2), Majiang–Heishuihe Fault Zone (F3), Xisha Trough Fault Zone (F4), northern boundary of the Central Basin (F5), mid-ocean ridge of the Central Basin (F6–F7), southern boundary of the Central Basin (F8), Tingjia Fault Zone (F9), Nansha Trough Southeastern Margin Fault Zone (F10), Sulu Sea Peripheral Fault Zone (F11), Celebes Sea Peripheral Fault Zone (F12), Manila Trench Subduction Zone (F13), Luson Trough Fault Zone (F14), Philippine Trench (F15), Ryukyu Trench (F16), Gagua Ridge (F17), Sabah–Palawan Fault (F18), Bukit Misin Fault Zone (F19), and Lupar Fault Zone (F20). These faults exhibit complex orientations, predominantly trending NE, NNE, NEE, and NW.

F1, located in the northern South China Sea, is the Littoral Fault Zone with a NEE strike. It extends westward to Hainan Island and is situated along the continent–ocean boundary. The offshore extension of the Red River Fault Zone in the South China Sea remains a subject of ongoing academic debate (Xue ZX et al., 2025b). In this study, fault F2, identified by the THASTG method, provides new high-resolution evidence pertinent to this issue. F2 originates from the Yinggehai Basin in the western part of Hainan Island, with its strike gradually transitioning from ES to NS and ultimately terminating in the Wan’an Basin with a NW orientation. This result not only corroborates the previous macroscopic interpretations (Xue ZX et al., 2021; Guo DM and Xue ZX, 2023) but also delineates its complete geometry and key inflection points with continuous and convergent boundaries. Compared with existing studies, the THASTG-derived result further clarifies the continuous distribution of the fault and its spatial relationship with adjacent structures. Its noise-resistant capability effectively reduces interpretational ambiguity in complex areas, thereby furnishing reliable new constraints for resolving this long-standing controversy. F3 is the Majiang–Heishuihe Fault Zone, which is situated between Indochina and the South China Sea. F4 is the Xisha Trough Fault Zone in the northern South China Sea, whose strike is approximately parallel to that of F1 and aligns closely with the continent–ocean boundary proposed by Zhang J et al. (2021) and Guo DM and Xue ZX (2023). F5 and F8 represent the northern and southern boundaries of the Central Basin, respectively. Together with F13 (Manila Trench Fault), they delineate the rhombic structure of the Central Basin (Guo DM and Xue ZX, 2023). F6 and F7 correspond to the NE-striking mid-ocean ridge within the Central Basin. Fault zones such as F11–F13 and F15–F18, resulting from plate subduction and collision, separate the marginal basins from the Pacific Plate (Karig, 1974; Zhang Y et al., 2016; Xue ZX et al., 2025b). F19 and F20 are located within the Natuna–Borneo fold-and-thrust belt, representing suture zones formed by subduction–collision events between the Nansha Block and Borneo (Hutchison, 1996, 2004).

5. Conclusion

In this study, an improved edge detection method termed THASTG is proposed, which enables the simultaneous identification of geological boundaries at varying depths while offering high localization accuracy and strong convergence. The method significantly suppresses noise interference, effectively enhances the resolution of the detection results, and avoids generating spurious boundaries. Notably, the THASTG method can effectively suppress residual noise during data processing. If the original data are of poor quality or contain strong interfering signals, we recommend performing appropriate preprocessing first to improve the signal-to-noise ratio, thereby ensuring reliable edge detection results.

The method is first tested using complex models under three different scenarios, and comparative analyses with other conventional methods confirm the reliability of the THASTG approach. Finally, the THASTG method is successfully applied to measured gravity data from the South China Sea region, yielding results largely consistent with previous findings.

In this study, 20 fault zones in the South China Sea region are identified on the basis of integrated gravity field model data, the extension characteristics of the Red River Fault Zone within this area are clarified, and the continent–ocean boundary position is delineated. The results significantly increase the precision and reliability of tectonic identification and provide important references for further understanding the tectonic evolution of the South China Sea.

Availability of Data and Materials

The ETOPO1 data and ICGEM website are available from https://www.ncei.noaa.gov/products/etopo-global-relief-model and https://icgem.gfz-potsdam.de/home. The China Seismic Active Fault Survey Data Center can be accessed at https://www.activefault-datacenter.cn/. The datasets used or generated in this study are available from the corresponding author on reasonable request.

Competing Interests

The authors declare that they have no competing interests.

Authors' contributions

In this study, Zhixin Xue and Lei Jing conceived and designed the method; Zhixin Xue, Longjun Qiu, and Jian Fang were responsible for the model data and real data analysis; and Zhixin Xue wrote the main manuscript text. All authors read and approved the final manuscript.

Acknowledgments

This work was financially supported by the National Natural Science Foundation of China (Grant Nos. 42474121, 42192535, and 42504055), the Surplus Funds from the Central Government Research Projects of the Institute of Geophysical and Geochemical Exploration (IGGE; Grant No. JY202505), the National Nonprofit Institute Research Grant of IGGE (Grant Nos. AS2025P02-1 and AS2024J10). We would like to express our gratitude to the editor and reviewers for the helpful comments to improve the manuscript. We would also like to acknowledge the use of the Generic Mapping Tools software (Wessel et al., 2013) for generating most of the figures in this study.

References

Amante, C., and Eakins, B. W. (2009). *ETOPO1 1 Arc-Minute Global Relief Model: Procedures, Data Sources and Analysis*. Boulder: National Geophysical Data Center.

Ariff, N. S. E., Olesen, A. K., Yaacob, N. M., and Sulaiman, S. A. H. (2021). Evaluation of gravity anomaly and geoid height derived from various global geopotential model. In *2021 IEEE 12th Control and System Graduate Research Colloquium (ICSGRC)* (pp. 34–39). Shah Alam, Malaysia: IEEE. https://doi.org/10.1109/ICSGRC53186.2021.9515205

Beiki, M. (2010). Analytic signals of gravity gradient tensor and their application to estimate source location. *Geophysics*, *75*(6), I59–I74. https://doi.org/10.1190/1.3484099

Cooper, G. R. J., and Cowan, D. R. (2006). Enhancing potential field data using filters based on the local phase. *Comput. Geosci.*, *32*(10), 1585–1591. https://doi.org/10.1016/j.cageo.2006.02.016

Cordell, L. (1979). Gravimetric expression of graben faulting in Santa Fe country and the Espanola Basin, New Mexico. In *New Mexico Geological Society Guidebook, 30th Field Conference* (pp. 59–64). Socorro: New Mexico Geological Society. https://doi.org/10.56577/FFC-30.59

Cordell, L., and Grauch, V. J. S. (1982). Mapping basement magnetization zones from aeromagnetic data in the San Juan Basin, New Mexico. In *SEG Technical Program Expanded Abstracts 1982* (pp. 246–247). Tulsa: Society of Exploration Geophysicists. https://doi.org/10.1190/1.1826915

Eldosouky, A. M., Pham, L. T., Mohmed, H., and Pradhan, B. (2020). A comparative study of THG, AS, TA, Theta, TDX and LTHG techniques for improving source boundaries detection of magnetic data using synthetic models: A case study from G. Um Monqul, North Eastern Desert, Egypt. *J. Afr. Earth Sci., 170*, 103940. https://doi.org/10.1016/j.jafrearsci.2020.103940

Ferreira, F. J. F., De Souza, J., de B. e S. Bongiolo, A., and de Castro, L. G. (2013). Enhancement of the total horizontal gradient of magnetic anomalies using the tilt angle. *Geophysics*, *78*(3), J33–J41. https://doi.org/10.1190/geo2011-0441.1

Guo, D. M., and Xue, Z. X. (2023). Depth distribution of Moho model and tectonic patterns in South China Sea and adjacent areas. *Heliyon*, *9*(5), e16281. https://doi.org/10.1016/j.heliyon.2023.e16281

Hayes, D. E., and Nissen, S. S. (2005). The South China Sea margins: Implications for rifting contrasts. *Earth Planet. Sci. Lett.*, *237*(3–4), 601–616. https://doi.org/10.1016/j.epsl.2005.06.017

Hu, S. X., Alves, T. M., Omosanya, K. O., and Li, W. (2021). Geometric and kinematic analysis of normal faults bordering continental shelves: A 3D seismic case study from the northwest South China Sea. *Mar. Petrol. Geol.*, *133*, 105263. https://doi.org/10.1016/j.marpetgeo.2021.105263

Hutchison, C. S. (1996). The 'Rajang accretionary prism' and 'Lupar Line' problem of Borneo. In *Geological Society, London, Special Publications 1996* (pp. 247–261). London: Geological Society of London. https://doi.org/10.1144/GSL.SP.1996.106.01.16

Hutchison, C. S. (2004). Marginal basin evolution: The southern South China Sea. *Mar. Petrol. Geol.*, *21*(9), 1129–1148. https://doi.org/10.1016/j.marpetgeo.2004.07.002

Karig, D. E. (1974). Evolution of arc systems in the western Pacific. *Annu. Rev. Earth Planet. Sci.*, *2*, 51–75. https://doi.org/10.1146/annurev.ea.02.050174.000411

Liang, W., Li, J. C., Xu, X. Y., Zhang, S. J., and Zhao, Y. Q. (2020). A high-resolution earth's gravity field model SGG-UGM-2 from GOCE, GRACE, satellite altimetry, and EGM2008. *Engineering, 6*(8), 860–878. https://doi.org/10.1016/j.eng.2020.05.008

Metcalfe, I. (2011). Tectonic framework and phanerozoic evolution of Sundaland. *Gondwana Res.*, *19*(1), 3–21. https://doi.org/10.1016/j.gr.2010.02.016

Miller, H. G., and Singh, V. (1994). Potential field tilt—A new concept for location of potential field sources. *J. Appl. Geophys.*, *32*(2–3), 213–217. https://doi.org/10.1016/0926-9851(94)90022-1

Paterson, N. R., and Reeves, C. V. (1985). Applications of gravity and magnetic surveys; the state-of-the-art in 1985. *Geophysics, 50*(12), 2558–2594. https://doi.org/10.1190/1.1441884

Pham, L. T., Van Vu, T., Le Thi, S., and Trinh, P. T. (2020). Enhancement of potential field source boundaries using an improved logistic filter. *Pure Appl. Geophys.*, *177*(11), 5237–5249. https://doi.org/10.1007/s00024-020-02542-9

Pham, L. T., Oksum, E., van Le, D., Ferreira, F. J. F., and Le, S. T. (2022). Edge detection of potential field sources using the softsign function. *Geocarto Int.*, *37*(14), 4255–4268. https://doi.org/10.1080/10106049.2021.1882007

Roest, W. R., Verhoef, J., and Pilkington, M. (1992). Magnetic interpretation using the 3-D analytic signal. *Geophysics*, *57*(1), 116–125. https://doi.org/10.1190/1.1443174

Sertcelik, I., and Kafadar, O. (2012). Application of edge detection to potential field data using eigenvalue analysis of structure tensor. *J. Appl. Geophys.*, *84*, 86–94. https://doi.org/10.1016/j.jappgeo.2012.06.005

Verduzco, B., Fairhead, J. D., Green, C. M., and MacKenzie, C. (2004). New insights into magnetic derivatives for structural mapping. *Lead. Edge*, *23*(2), 116–119. https://doi.org/10.1190/1.1651454

Wessel, P., Smith, W. H. F., Scharroo, R., Luis, J., and Wobbe, F. (2013). Generic mapping tools: Improved version released. *EoS, Trans. AGU*, *94*(45), 409–410. https://doi.org/10.1002/2013EO450001

Wijns, C., Perez, C., and Kowalczyk, P. (2005). Theta map: Edge detection in magnetic data. *Geophysics*, *70*(4), L39–L43. https://doi.org/10.1190/1.1988184

Wu, X. Y., Xu, X. W., Yu, G. H., Ren, J. J., Yang, X. P., Chen, G. H., Xu, C., Du, K. P., Huang, X. N., … Hao, H. J. (2024). The China Active Faults Database (CAFD) and its web system. *Earth Syst. Sci. Data*, *16*(7), 3391–3417. https://doi.org/10.5194/essd-16-3391-2024

Xue, Z. X., Guo, D. M., Li, H. L., and Zhang, P. P. (2021). Analysis on Bouguer gravity anomaly characteristics and boundary identification in China and surrounding regions. *Terr. Atmos. Ocean. Sci.*, *32*, 797–812. https://doi.org/10.3319/TAO.2021.06.22.02

Xue, Z. X., Fang, J., Guo, D. M., and Zhang, P. P. (2025a). Characterization of the tectonic structures on the Tibetan Plateau using gravity anomaly data and an improved edge detection method. *Earth Planets Space*, *77*(1), 95. https://doi.org/10.1186/s40623-025-02232-7

Xue, Z. X., Guo, D. M., Fang, J., and Cui, R. H. (2025b). Constrained gravity inversion unravels the Moho depth and tectonic patterns in China and its adjacent areas. *Earth Planet. Phys.*, *9*(4), 799–816. https://doi.org/10.26464/epp2025043

Yuan, Y., Gao, J. Y., and Chen, L. N. (2016). Advantages of horizontal directional Theta method to detect the edges of full tensor gravity gradient data. *J. Appl. Geophys.*, *130*, 53–61. https://doi.org/10.1016/j.jappgeo.2016.04.009

Zhang, J., Yang, G. L., Tan, H. B., Wu, G. J., and Wang, J. P. (2021). Mapping the Moho depth and ocean-continent transition in the South China Sea using gravity inversion. *J. Asian Earth Sci.*, *218*, 104864. https://doi.org/10.1016/j.jseaes.2021.104864

Zhang, X., Yu, P., Tang, R., Xiang, Y., and Zhao, C. J. (2015). Edge enhancement of potential field data using an enhanced tilt angle. *Explor. Geophys.*, *46*(3), 276–283. https://doi.org/10.1071/EG13104

Zhang, Y., Li, S. Z., Suo, Y. H., Guo, L. L., Yu, S., Zhao, S. J., Somerville, I. D., Guo, R. H., Zang, Y. B., … Mu, D. L. (2016). Origin of transform faults in back-arc basins: Examples from Western Pacific marginal seas. *Geol. J.*, *51*(S1), 490–512. https://doi.org/10.1002/gj.2807

Zhou, S., Yao, X. A., Zeng, X. C., Dong, S. Y., and Yu, Z. Y. (2024). Magnetic data edge detection method with depth information based on UNet++. *IEEE Trans. Geosci. Remote Sens.*, *62*, 5933913. https://doi.org/10.1109/TGRS.2024.3490660

Zhou, X. Y., Chen, Z. X., Chen, H., Wang, S., and Kubeka, Z. O. (2024). Edge detection of source body from magnetic anomaly based on ResNet. *Remote Sens.*, *16*(22), 4139. https://doi.org/10.3390/rs16224139